



**HAL**  
open science

# The Complex Exhumation History of Jezero Crater Floor Unit and Its Implication for Mars Sample Return

C. Quantin-Nataf, S. Alwmark, F. J. Calef, J. Lasue, K. Kinch, K. M. Stack, V. Sun, N. R. Williams, E. Dehouck, L. Mandon, et al.

► **To cite this version:**

C. Quantin-Nataf, S. Alwmark, F. J. Calef, J. Lasue, K. Kinch, et al.. The Complex Exhumation History of Jezero Crater Floor Unit and Its Implication for Mars Sample Return. *Journal of Geophysical Research: Planets*, 2023, 128, 10.1029/2022JE007628 . insu-04473182v1

**HAL Id: insu-04473182**

**<https://insu.hal.science/insu-04473182v1>**

Submitted on 13 Mar 2024 (v1), last revised 17 Sep 2024 (v2)

**HAL** is a multi-disciplinary open access archive for the deposit and dissemination of scientific research documents, whether they are published or not. The documents may come from teaching and research institutions in France or abroad, or from public or private research centers.

L'archive ouverte pluridisciplinaire **HAL**, est destinée au dépôt et à la diffusion de documents scientifiques de niveau recherche, publiés ou non, émanant des établissements d'enseignement et de recherche français ou étrangers, des laboratoires publics ou privés.

Copyright

# JGR Space Physics











## RESEARCH ARTICLE

10.1029/2023JA031353

## Photoelectron Boundary: The Top of the Dayside Ionosphere at Mars

### Key Points:

- Large gradients in planetary ion density occur across the photoelectron boundary (PEB) and the PEB falls within the ion composition boundary
- The PEB can be considered as the top of the Mars dayside ionosphere
- The PEB is not a pressure balance boundary but is located where the shocked sheath flow is diverted around the ionosphere

Shaosui Xu<sup>1</sup> , David L. Mitchell<sup>1</sup> , James P. McFadden<sup>1</sup>, Christopher M. Fowler<sup>2</sup> , Kathleen Hanley<sup>1</sup> , Tristan Weber<sup>3</sup> , David A. Brain<sup>4</sup> , Yingjuan Ma<sup>5</sup> , Gina A. DiBraccio<sup>3</sup> , Christian Mazelle<sup>6</sup> , and Shannon M. Curry<sup>1</sup> 

<sup>1</sup>Space Sciences Laboratory, University of California, Berkeley, CA, USA, <sup>2</sup>Department of Physics and Astronomy, West Virginia University, Morgantown, WV, USA, <sup>3</sup>Goddard Space Flight Center, Greenbelt, MD, USA, <sup>4</sup>Laboratory for Atmospheric and Space Physics, University of Colorado, Boulder, CO, USA, <sup>5</sup>Department of Earth, Planetary, and Space Sciences, University of California, Los Angeles, CA, USA, <sup>6</sup>IRAP, CNRS - University of Toulouse - UPS - CNES, Toulouse, France

### Supporting Information:

Supporting Information may be found in the online version of this article.

### Correspondence to:

S. Xu,  
[shaosui.xu@ssl.berkeley.edu](mailto:shaosui.xu@ssl.berkeley.edu)

### Citation:

Xu, S., Mitchell, D. L., McFadden, J. P., Fowler, C. M., Hanley, K., Weber, T., et al. (2023). Photoelectron boundary: The top of the dayside ionosphere at Mars. *Journal of Geophysical Research: Space Physics*, 128, e2023JA031353. <https://doi.org/10.1029/2023JA031353>

Received 27 JAN 2023

Accepted 2 MAY 2023

**Abstract** The interaction between Mars and the solar wind results in different plasma regimes separated by several boundaries, among which the separation between the sheath flow and the ionosphere is complicated. Previous studies have provided different and sometimes opposite findings regarding this region. In this study, we utilize observations from the Mars Atmospheric and Volatile Evolution (MAVEN) mission to revisit boundaries within this region and perhaps reconcile some differences. More specifically, we start with the photoelectron boundary (PEB), a topological boundary that separates magnetic field lines having access to the dayside ionosphere (open or closed) from those connected to the solar wind on both ends (draped). We find that large gradients in the planetary ion density occur across the PEB and that the dominant ion switches from heavy planetary ions to protons near the PEB, indicating that the PEB falls within the ion composition boundary (ICB). Furthermore, our results show that the PEB is not a pressure balance boundary; rather the magnetic pressure dominates both sides of the PEB. Meanwhile, we find that the PEB is located where the shocked solar wind flow stops penetrating deeper into the ionosphere. These findings suggest the PEB marks the top of the Mars dayside ionosphere and also the interface where the sheath plasma flow deflects around the obstacle going downstream.

## 1. Introduction

For a planetary object without a significant global dipole field but with a significant atmosphere, like Venus and Mars, its ionosphere acts as the main obstacle to the solar wind. Mars's localized crustal fields (Acuña et al., 1998; Connerney et al., 2005), which are strong enough in some locations to stand off the solar wind at altitudes well above the ionosphere and form miniature crustal magnetospheres, also contribute significantly to this interaction. Nonetheless, to the first approximation, these two planets' interaction with the solar wind results in similar plasma regimes separated by several boundaries (Luhmann, 1986; Nagy et al., 2004). A bow shock is formed that separates the upstream solar wind and the magnetosheath populated with the shocked solar wind. Together with flow stagnation and deflection downstream of the bow shock, mass loading enhances the interplanetary magnetic field (IMF) pileup over the dayside ionosphere, forming a magnetic barrier, separated from the magnetosheath by a magnetic pileup boundary (MPB; or the induced magnetospheric boundary [Bertucci et al., 2012]). Near or below the MPB, a boundary commonly observed at both Venus and Mars is the ion composition boundary (ICB), which marks the change of dominant ion species from solar wind to planetary origin (e.g., Bertucci et al., 2012; Halekas et al., 2018; Holmberg et al., 2019; Matsunaga et al., 2017; Xu et al., 2016).

An important difference between Venus and Mars in terms of plasma boundaries is whether there exists an ionopause that clearly separates the unmagnetized ionosphere from the magnetic barrier. During solar maximum, the Venusian ionosphere is strong enough (the ionospheric thermal plasma pressure at or above the exobase is higher than the impinging solar wind dynamic pressure) to stand off solar wind penetration (e.g., Luhmann, 1986). An ionopause is formed as a result of pressure balance, characterized by sharp gradients in both ionospheric density and magnetic field strength. At Mars, the ionosphere is much weaker and generally unable to prevent IMF penetration above the exobase. There are still regions of localized density gradients at Mars, but they are not always ionopause-like (i.e., no corresponding gradient in magnetic pressure; Chu et al., 2021, 2019; Duru et al., 2009;

Sánchez-Cano et al., 2020; Vogt et al., 2015). The consensus is that the concept of the ionopause as seen at Venus is usually not applicable to Mars.

Below the MPB, at both Mars and Venus, a distinct and often sharp boundary is observed that separates ionospheric photoelectrons (produced by solar photons ionizing the neutral atmosphere) and solar wind electrons, termed the “photoelectron boundary” (PEB; Dubinin et al., 2006; Frahm et al., 2006; Garnier et al., 2017; Mitchell et al., 2001; Wang et al., 2022). The interpretation is that the PEB is a topological boundary that separates the draped IMF from field lines connected to the ionospheric production region. The PEB is often observed to coincide with sharp density gradients at Mars (Duru et al., 2009). The general properties of the PEB have been investigated in several studies, including its altitude increasing with crustal field strength, extreme ultraviolet intensity and solar zenith angle (SZA; Garnier et al., 2017; Wang et al., 2022).

Observationally, MPB, ICB, and PEB are reported to be closely located spatially but their relations with respect to each other might differ depending on the specific definitions of these boundaries in different studies, which we will discuss in further detail later. In this study, we examine properties at or near the PEB, revisit the relation between this boundary and ICB and ionopause, and explore the physical nature of this boundary. Previous studies determined the location of the PEB based on pitch-angle averaged electron energy distributions (e.g., Duru et al., 2009; Garnier et al., 2017), from which magnetic topology cannot be unambiguously determined. This study adopts the methodology of Xu et al. (2019) to accurately determine magnetic topology based on observed electron pitch angle and energy distributions, allowing for a more accurate determination of the PEB. The paper is organized as follows: we present a case study in Section 2, followed by the characterization of general properties of the PEB in Section 3; we then explore the physical nature of the PEB in Section 4 and provide a physical interpretation of our observational results in Section 5, followed by a discussion in Sections 6; lastly, we conclude the paper in Section 7.

## 2. Case Study

We illustrate a few key parameters examined in this study via a case study first on 12 July 2017, as shown in Figure 1. Mars Atmospheric and Volatile Evolution (MAVEN) observations included in this study are suprathermal electron measurements from the Solar Wind Electron Analyzer (SWEA; Mitchell et al., 2016), ion measurements from the SupraThermal And Thermal Ion Composition (STATIC) instrument (McFadden et al., 2015), and magnetic field vectors measured by the Magnetometer (Connerney et al., 2015). From top to bottom, Figure 1 shows the time series of ion energy spectra for all masses (a) and for ion mass ( $M$ ) < 10 amu (b) measured by STATIC, (c) calculated characteristic light ( $M$  < 10 amu) ion velocity ( $V_c$ ), (d) the derived ion densities from STATIC measurements using necessary calibrations provided by Fowler et al. (2022b), (e) magnetic field amplitude measured by MAG, (f) normalized electron pitch angle distribution for 111–140 eV, and (g) omnidirectional electron energy spectra measured by SWEA, and (h) spacecraft altitude colored by magnetic topology.

The characteristic velocity of light ions,  $V_c$ , is calculated based on the ion energy spectra for ion mass < 10 amu (as shown in panel b) measured by STATIC. More specifically,

$$V_c = \frac{\sum j(E) \Delta E}{\sum j(E) / \sqrt{2E} / m_p \Delta E} \quad (1)$$

where  $j(E)$  is the differential ion number flux and  $m_p$  is the proton mass. Essentially,  $V_c$  is the integrated ion number flux divided by a density-equivalent quantity, thus a mixture of proton bulk velocity and thermal velocity but with no directional information. Ideally, we would want to examine the flow velocity vector near the PEB. However, MAVEN starts to rotate from ~1000 to 500 km altitude, which is not optimized for either STATIC or the Solar Wind Ion Analyzer instrument (Halekas et al., 2015) to observe the full ion distribution. It makes it very complicated to obtain the ion velocity and we thus use  $V_c$  instead. Figure S1 in Supporting Information S1 maps the median  $V_c$  in different projections: the MSO (Mars-centered Solar Orbit)  $X$ - $Y$ ,  $X$ - $Z$ , and also the cylindrical  $X$ - $\rho$  plane, where  $\rho = \sqrt{Y^2 + Z^2}$ . In MSO, the  $X$ -axis points from the center of Mars to the Sun, the  $Z$ -axis points to the ecliptic north pole of Mars's orbital plane, and the  $Y$ -axis completes the right-handed system. As shown in Figure S1 in Supporting Information S1,  $V_c$  captures the high solar wind flow velocity upstream of the bow shock, transitions to a slower and hot flow in the sheath, and then turns to cold and slow near the planet. This fits the typical picture of the solar wind flow around Mars and validates the usage of this quantity.

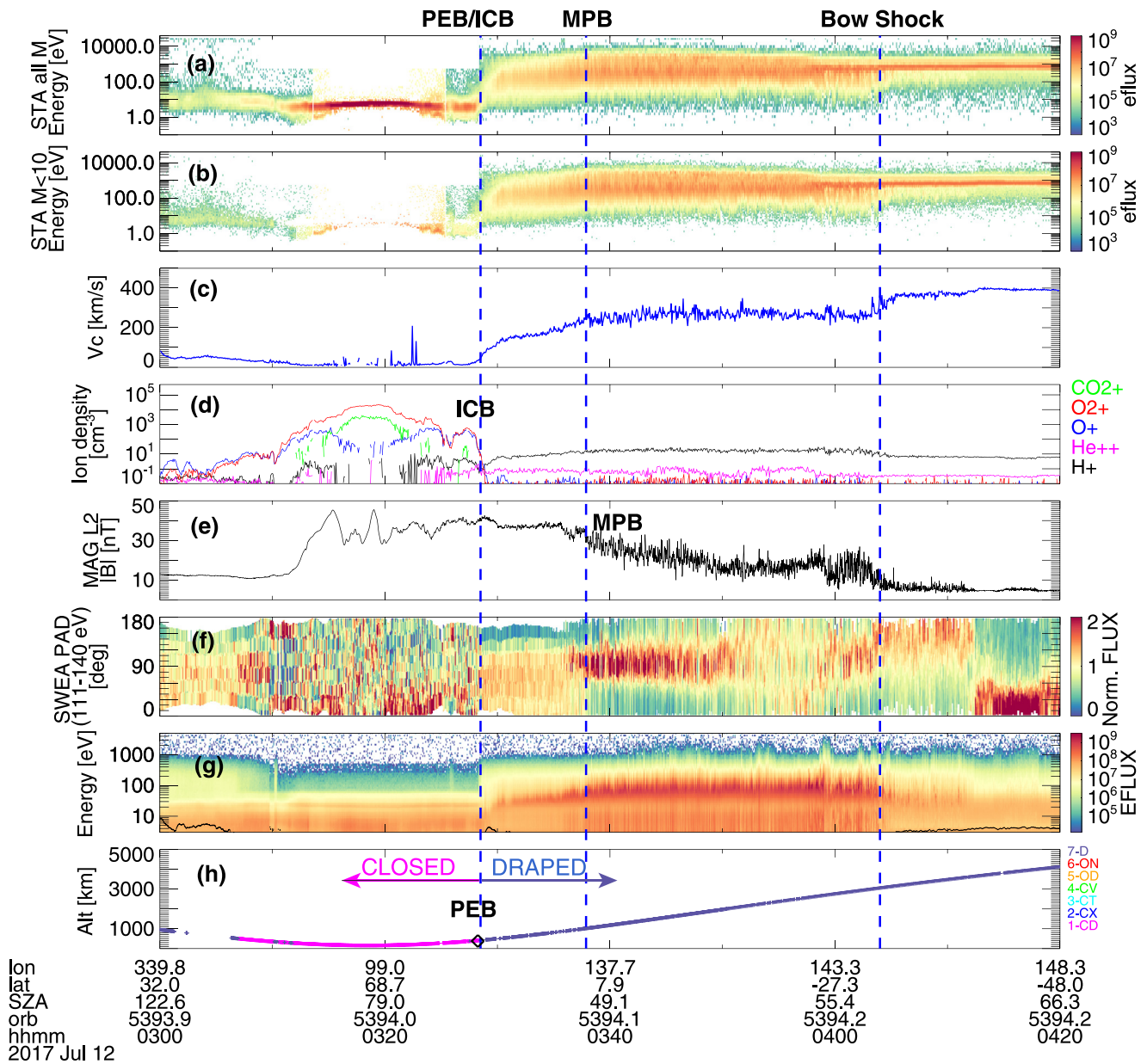


**Figure 1.** Time series of Mars Atmospheric and Volatile Evolution observations on 12 July 2017. From top to bottom: ion energy spectra for all masses (a) and for ion mass < 10 amu (b) measured by SupraThermal And Thermal Ion Composition (STATIC), (c) calculated characteristic light ( $M < 10$  amu) ion velocity  $V_c$ , (d) the derived ion densities from STATIC measurements, (e) magnetic field amplitude measured by MAG, (f) normalized electron pitch angle distribution for 111–140 eV, and (g) omnidirectional electron energy spectra measured by electron energy spectra (SWEA), and (h) spacecraft altitude colored by magnetic topology. The diamond symbol in h marks the PEB location identified from the automated procedure. A few key boundaries are marked as the vertical dashed lines.

Magnetic topology in panel (h) is determined based on the methodology described in Xu et al. (2019). Seven types of magnetic topology can be distinguished: (a) closed field lines with both ends in the dayside ionosphere (closed-day), (b) cross-terminator closed field lines with one end in the dayside ionosphere and the other in the nightside ionosphere (closed-terminator), (c) closed field lines with both ends in the nightside ionosphere with trapped electrons (closed-trapped), (d) closed field lines with both ends in the nightside ionosphere with superthermal electron depletions (closed-void), (e) open field lines connected to the dayside ionosphere on one end and to the solar wind on the other end (open-day), (f) open field lines connected to the nightside ionosphere and the solar wind on the other end (open-night), and (g) draped with both ends connected back to the solar wind (and not intersecting the ionosphere).

From right to left (reverse time order) of Figure 1, the MAVEN spacecraft encountered the bow shock at ~04:04:00 UT (universal time), indicated by the transition from the cold solar wind ion beam to the hot magnetosheath ion flow (panels a, b), enhanced electron fluxes at high energies (panel g), and the increase in magnetic field strength and fluctuation (panel e). At ~03:37:50 UT, the ramp-up in magnetic field strength and the reduction in magnetic fluctuation in panel e and the decreased electron fluxes above 100 eV in panel g indicate the crossing of the MPB (e.g., Bertucci et al., 2005; Crider et al., 2000). At ~03:28:30 UT, in panel d, steep density gradients in heavy ions ( $O^+$  and  $O_2^+$ ) and also the switch of the dominant ion species from  $H^+$  to heavy ions indicate the crossing of the ICB. At the same time, we observe a magnetic topology change from draped topology (blue) to closed field (magenta) in panel h, indicating the crossing of the PEB. Lastly, in panel c, the characteristic velocity  $V_c$  varies from ~400 km/s upstream of the bow shock, to ~270 km/s in the sheath between the MPB and the bow shock, to ~200 km/s below the MPB between 03:30 UT and 03:35 UT, and then quickly decreases to near 0 from 03:30 UT to 03:25 UT across the PEB.

Figure 2 shows another example of MAVEN observations on 21 June 2017, where the crossings of the MPB, PEB, and ICB are at SZA ~27°–29°, much closer to the subsolar region. This case study exhibits similar features as the previous example: the MPB is located well above the PEB and ICB while the ICB and PEB are co-located. Meanwhile, there are cases where these three boundaries are located at similar locations as all plasma regimes are more compressed at the subsolar region than higher SZAs. It is worth noting that technically all boundaries have a thickness of different scales and the exact locations of these boundaries may vary depending on specific definitions. As illustrated later, our analysis does not rely on the most accurate determination of the boundary locations but focuses on the physical interpretation of the relations between these boundaries.

To summarize observations worth highlighting in the vicinity of the PEB in both case studies: (a) in panel c,  $V_c$  approaches small values, a few tens of km/s; (b) in panel d, steep density gradients of heavy ions are observed; (c) in panel d, the dominant ion species changes from  $H^+$  to heavy ions; (d) in panel e, no obvious magnetic gradient occurs at this boundary. Through statistical analyses shown in later sections, we demonstrate that these are common features near the PEB and that the PEB can thus be considered as the top of the dayside ionosphere at Mars.

### 3. General Properties of the PEB

To conduct statistical analyses, we design an automated procedure to identify the PEB based on magnetic topology. More specifically, for every inbound and outbound orbit segment centered on periapsis, we search for the highest altitude (98%-rank) of all topologies having access to the dayside ionosphere, including Topology 1 “closed-to-day”, 2 “cross-terminator-closed”, and 5 “open-to-day” (“open-to-day” also having access to the solar wind). Here, we define the X%-rank of a distribution (altitude in this case) such that X% of the distribution falls below that value. The PEB identified by this automated procedure is marked as the diamond symbol in Figures 1h and 2h, which agrees very well with the visual inspection. We search through MAVEN orbits from 1 February 2016 to 1 April 2020 and bound this search to dayside (SZA < 90°) and altitudes between 150 and 2000 km, which results in 7013 PEB identifications combining the inbound and outbound segments.

The properties of the PEB have been investigated in several studies (Frahm et al., 2006; Garnier et al., 2017; Wang et al., 2022), including the effects of the upstream dynamic pressure, solar irradiance, and crustal magnetic fields. Here, as our definition of the PEB is topological, we examine two common features with our selected PEBs, as shown in Figure 3. In panel a, the median PEB altitude in the Mars geographic coordinates shows a clear dependence on the crustal magnetic field strength, varying from ~600 km over weak crustal fields to up to 1200 km over strongest crustal fields, which is consistent with previous studies (Garnier et al., 2017; Wang et al., 2022). Note that this map folds in the dependence of the PEB altitude on SZA, as high geographic latitudes, at which the strongest crustal fields are located, are generally located at high SZAs. In panel b, the median PEB altitude (black line) increases from ~500 to 600 km at low SZAs to ~1000 km at high SZAs. This is because the component of the solar wind dynamic pressure normal to the boundary surface scales roughly as  $\cos^2(\text{SZA})$ , and plasma boundaries tend to flare away from the planet at high SZAs (e.g., Halekas et al., 2018). The blue and red lines are median PEB altitudes for  $|B_c| < 10$  nT and  $|B_c| > 10$  nT, respectively, where  $|B_c|$  is the model crustal field strength at 400 km altitude (Morschhauser et al., 2014). The median PEB altitude varies from <500 km to ~1000 km for  $|B_c| < 10$  nT and from <700 km to ~1200 km for  $|B_c| > 10$  nT, having an offset of 200–300 km altitude between these two scenarios.



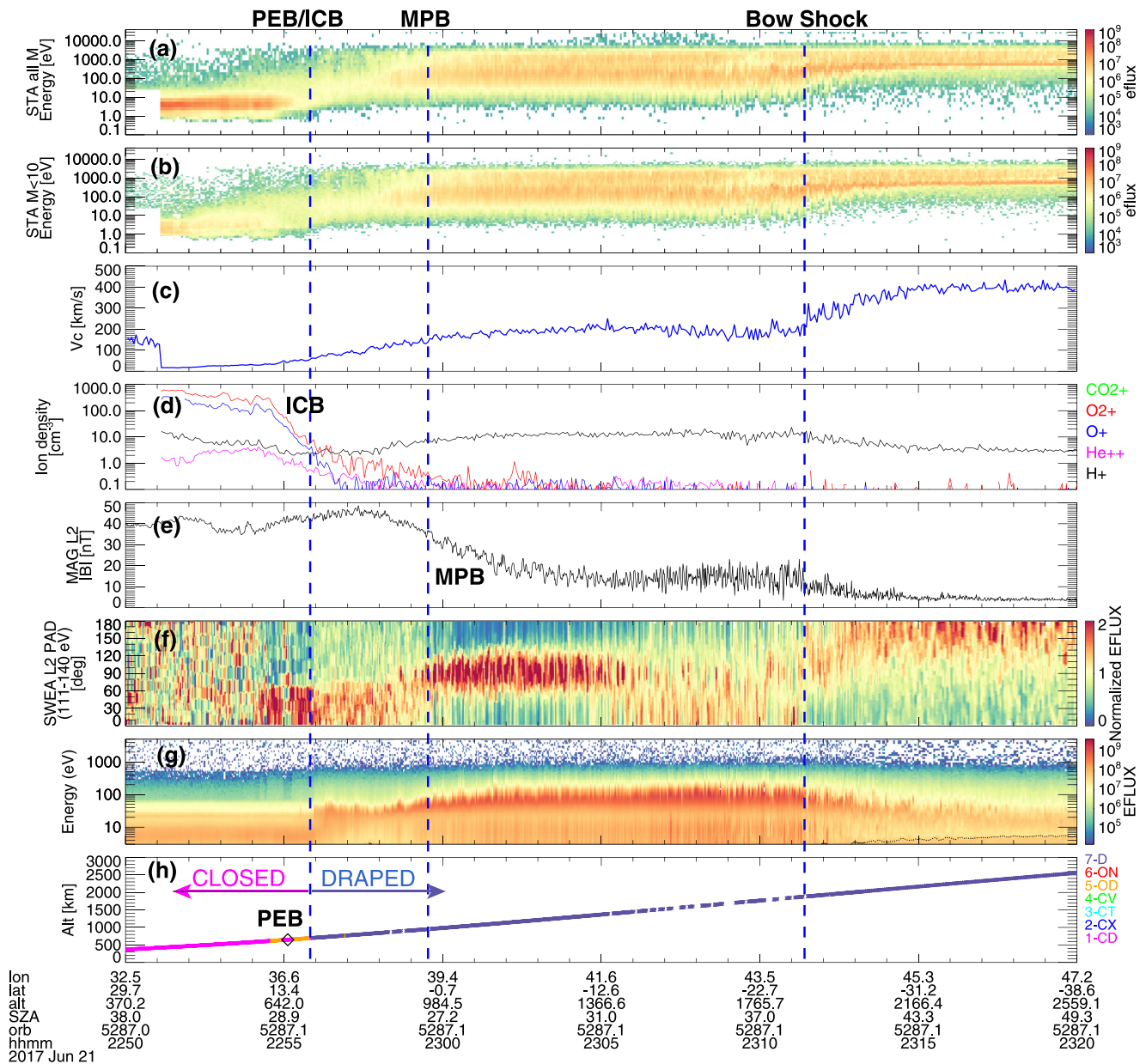


Figure 2. Time series of Mars Atmospheric and Volatile EvolutionN observations on 21 June 2017, the same format as Figure 1.

## 4. Physical Nature of the PEB

In this section, we investigate the physical nature of the PEB from: (a) the relation between the PEB and ion density gradients; (b) the relation between the PEB and ion composition changes; (c) whether balance between different pressure terms defines the location of the PEB (as it does for the traditional ionopause); (d) the variation of the characteristic velocity of the sheath flow near the PEB. Note that the region below MPB (where the PEB is generally located) is considered by many authors to be separated from the magnetosheath, but we use the term “the sheath flow” to refer to shocked solar wind plasma above the planetary ionosphere for simplicity.

### 4.1. PEB and Heavy Ion Density Gradients

The case studies in Section 2 show that steep density gradients in  $O^+$  and  $O_2^+$  are observed at the PEB. In this subsection, we investigate whether this is a common feature of the PEB through statistical analyses.

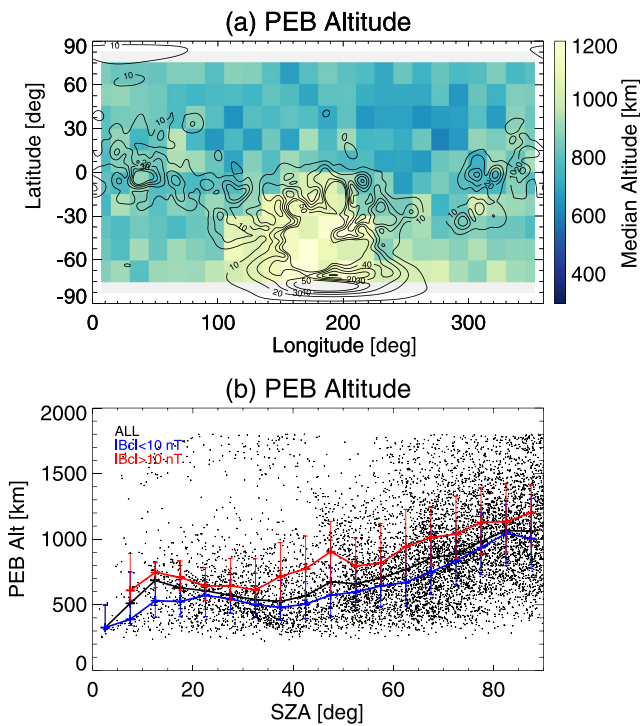


**Figure 3.** (a) Median photoelectron boundary (PEB) altitudes in geographic latitude and longitude, overlaid with the contours of modeled crustal field strengths ( $|B_{cl}|$  in nT) at 400 km altitude (Morschhauser et al., 2014). (b) PEB altitudes against SZA, “+” for all identified PEBs, black, blue, and red lines for median PEB altitudes for all PEBs,  $|B_{cl}| < 10$  nT, and  $|B_{cl}| > 10$  nT, respectively. The error bars are interquartiles.

To examine the ion density gradient, we define an ion scale height  $H_{i^+}$  as  $1/H_{i^+} = -\Delta \log(n_{i^+})/\Delta z$ , where  $n_{i^+}$  is the ion density and  $z$  is altitude. Practically,  $H_{i^+}$  is calculated based on the best linear fit of  $\log(n_{i^+})$  and  $z$  within an altitude range. The concept of a scale height implies hydrostatic equilibrium, which is not necessarily applicable for ions at high altitudes, but here we use it to characterize ion density gradient for convenience. We separately calculate ion scale heights for both  $O^+$  and  $O_2^+$  at and below the PEB for each identified PEB. Here, we define “at PEB” to be  $[z_p - 25, z_p + 25]$  km and “below PEB” to be  $[z_p - 175, z_p - 125]$  km to examine characteristics of plasma across the PEB and in the nominal ionosphere, where  $z_p$  is the PEB altitude. Figures 4a and 4b show  $H_{O^+}$  and  $H_{O_2^+}$  against the PEB altitude ( $z_p$ ) at and below the PEB. Note that there is no  $H_{O^+}$  for  $z_p < 350$  km altitude as  $H_{O^+}$  is negative below its density peak ( $\sim 250$  km; Fowler et al., 2022b) and thus not counted here. In both panels,  $H_{O^+}$  and  $H_{O_2^+}$  increase with altitude, likely because ion scale heights are smaller close to the production region and larger at high altitudes where plasma diffusion dominates and/or ion temperatures increase with altitude. For  $O^+$ , the median  $H_{i^+}$  is 20–40 km at the PEB and  $\sim 60$  km below the PEB, which translates to a density change over 100 km altitude of a factor of  $\sim 150$ –12 at the PEB and of a factor of  $\sim 5$  below the PEB. For  $O_2^+$ , the median  $H_{i^+}$  is 15–28 km at the PEB and 30–60 km below the PEB, which translates to a density change over 100 km altitude of a factor of 786–28 at the PEB and of a factor of 28–5 below the PEB. Overall, the ion scale height at the PEB is about half of that below the PEB (Figure 4c). In other words, across the PEB, the ion density profiles are distinctively different from those below, having a more prominent decrease with altitude.

Another approach to examining density, composition, and magnetic field gradients around the PEB is to normalize each of these parameters to its value at the PEB. The median profiles of the normalized  $H^+$ ,  $O^+$ , and  $O_2^+$  densities, the heavy-to-light ion density ratio, and the magnetic field amplitude are shown as a function of altitude relative to the PEB ( $z - z_p$ ) in Figure 5.

The lower and upper quartiles of each profile are shown in Figure S2 in Supporting Information S1. The  $H^+$  density profile (black line) varies by less than a factor of two over 600 km altitude, the same as the case studies. In contrast, both  $O^+$  (blue line) and  $O_2^+$  (red line) densities vary by two orders of magnitude across the PEB, in comparison to a more gradual density change 150–200 km below the PEB. Similarly, we calculate  $H_{i^+}$  for  $[z_p - 50, z_p + 50]$  (across the PEB) and  $[z_p - 300, z_p - 200]$  (below the PEB), given in the upper right corner. Note that we use slightly different altitude intervals here than those used for each PEB crossing to better characterize ion density profiles in Figure 5. We see an  $H_{O^+}$  of 57 and 251 km and an  $H_{O_2^+}$  of 53 and 148 km, corresponding to a factor of  $\sim 5$  change in density at the PEB and less than a factor of two change below the PEB over 100 km altitude, respectively. In other words, both Figures 4 and 5 demonstrate that large density gradients in  $O^+$  and  $O_2^+$  are a common feature at the PEB, compared to much smaller density gradients below (and above) the PEB.

#### 4.2. PEB and ICB

Next, we examine the relationship between the PEB and ICB by taking into account their respective thickness. The ICB is the transition of the dominant ion from solar wind protons to planetary ions. Observationally, ICB has been defined as the location where the ratio of the proton density and heavy ion density is unity (e.g., Holmberg et al., 2019; Matsunaga et al., 2017) or by fitting the density ratio profile (Halekas et al., 2018). As pointed out by Halekas et al. (2018), the ICB is a boundary layer with a thickness that scales with the proton (convective and thermal) gyroradius (tens of km to hundreds of km on the dayside). In contrast, the PEB is a topological boundary that we probe with sub-keV electrons with gyroradii of order 1 km. In many cases, the PEB is effectively unresolved at the 2-s SWEA measurement cadence, corresponding to a thickness of less than a few km.

We, therefore, calculate the density ratio,  $\frac{n(O^+) + n(O_2^+)}{n(H^+)}$ , within 50 km of the PEB and bound this value by the

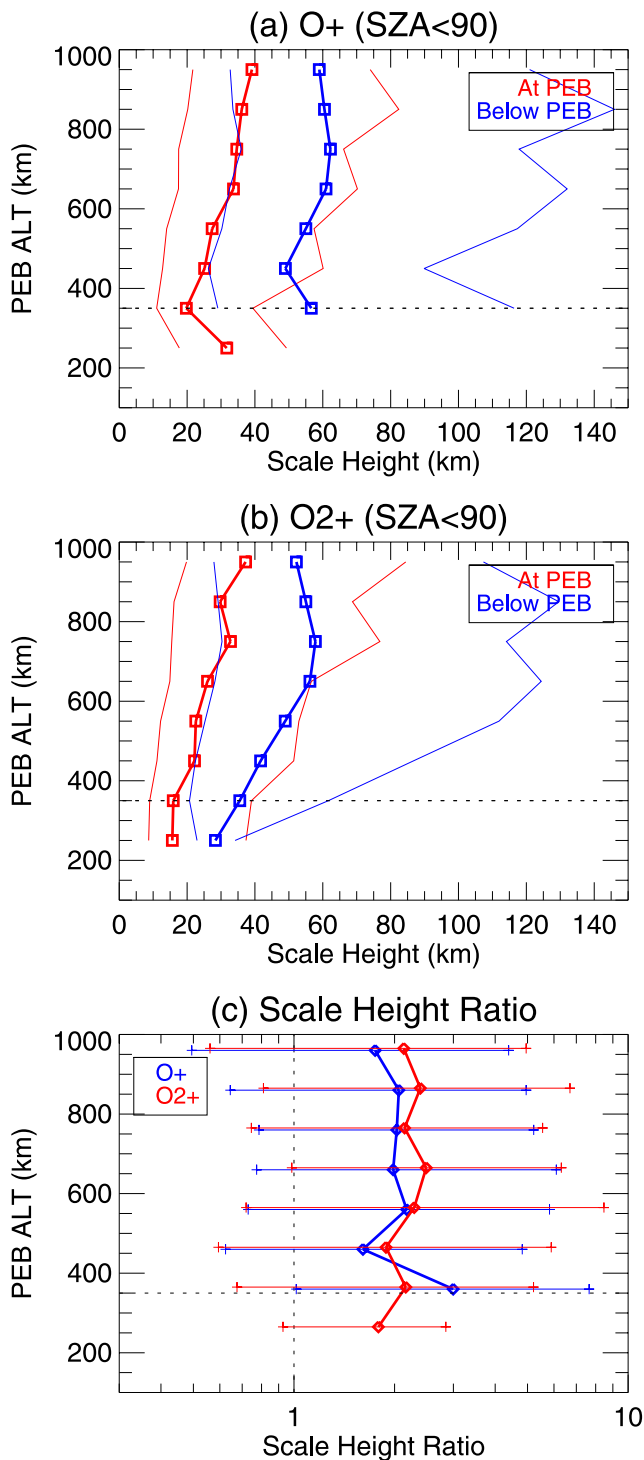


**Figure 4.** (a) Ion scale height for  $O^+$  ( $H_{O^+}$ ), thick red and blue lines (thin lines for lower and upper quartiles) are median  $H_{O^+}$  for at the photoelectron boundary (PEB) and below the PEB, respectively. (b) Ion scale height for  $O_2^+$  ( $H_{O_2^+}$ ), the same format as panel (a). (c) The median ratios of scale heights below the PEB to that at the PEB for  $O^+$  (blue) and  $O_2^+$  (red) and the error bars are interquartiles.

5%-rank and 95%-rank density ratio to represent the minimum and maximum density ratios near the PEB, respectively, for each PEB crossing. This avoids skewing the results by extreme outliers. The distributions of 5%-rank and 95%-rank density ratios are shown as blue and red lines in Figure 6. The median values of the minimum and maximum density ratios are 1.5 and 9.8, which are smaller than the peak values because of the usage of a logarithmic scale. It means that within the PEB  $\pm 50$  km altitude, the density ratio varies significantly and the dominant ions change from planetary ions (density ratio  $\gg 1$ ) to protons (density ratio  $\sim 1$ ). We, therefore, conclude that the PEB falls within the ICB considering the thickness of the latter boundary. Note that, in Figure 6, both distributions have a large spread of density ratios and the minimum ratio (blue line) is  $> 1$  more than half of the time. It is likely because the thickness of ICB varies and the PEB can be located at different portions of this compositional boundary layer. Similarly, the median density ratio,  $\frac{n(O^+) + n(O_2^+)}{n(H^+)}$ , for all the PEB crossings, as a function of altitude is overlaid as the cyan line in Figure 5. It displays a ratio of  $\sim 100$  below the PEB, dominated by heavy ions, and a ratio of  $\ll 1$  above the PEB, showing a much clearer ion compositional change across the PEB.

Sections 4.1 and 4.2 illustrate that large density gradients occur across the PEB and the PEB is contained within the much thicker ICB. We conclude that the PEB can be interpreted as the top of the dayside Mars ionosphere, which separates cold planetary ionospheric ions from the hot solar-wind-origin plasma.

### 4.3. PEB and Pressure Balance

In the classic picture (as observed at Venus), the dayside MPB and the ionopause result from a balance between different pressure terms. The MPB is located where the sheath plasma thermal pressure above balances the magnetic pressure ( $P_B$ ) below. Similarly, the ionopause is located where the magnetic pressure above balances the ionospheric plasma thermal pressure ( $P_{th}$ ) below. We consider the PEB to be the top of the dayside ionosphere, similar to the ionopause, and thus ask whether a balance between  $P_B$  and  $P_{th}$  applies at the PEB.  $P_B$  can be easily calculated from magnetic field measurements.

It is more complicated to obtain  $P_{th}$ , for which we need to know densities and temperatures of  $O^+$ ,  $O_2^+$ ,  $H^+$ , and  $e^-$  for both the cold and hot plasma populations, as the PEB marks the transition from the hot sheath plasma (mainly  $H^+$ ) to cold planetary plasma (mainly  $O^+$  and  $O_2^+$ ). For sheath electrons and ions above the PEB, the densities and temperatures must be determined from SWEA and STATIC/SWIA measurements. However, the PEB is located close to where the MAVEN spacecraft and articulated payload platform (APP) change their orientations in preparation for the upcoming periapsis pass. This reorientation can cause a significant part of the sheath plasma population to fall outside the fields of view of STATIC and/or SWIA, which prevents us from calculating reliable ion density and temperature moments. Obtaining electron moments is also complicated by the removal of secondaries produced within the SWEA instrument by intense sheath electron fluxes. Despite these limitations, it is known that the plasma thermal and dynamic pressures below the MPB are much smaller than the magnetic pressure, so we forgo this calculation and assume that  $P_B$  dominates between the PEB and the MPB.



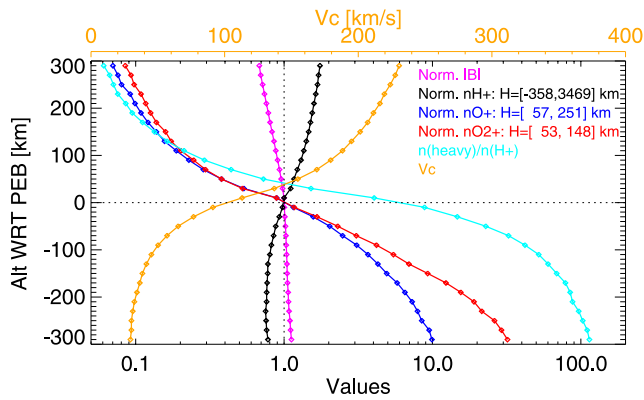


**Figure 5.** Normalized profiles of different parameters to values at the photoelectron boundary (PEB) against altitude relative to the PEB ( $z - z_p$ ), black for  $n(H^+)$ , blue for  $n(O^+)$ , red for  $n(O_2^+)$ , and magenta for  $|B|$ . The cyan line is the median density ratio of heavy ions to protons  $\left(\frac{n(O^+) + n(O_2^+)}{n(H^+)}\right)$  against  $z - z_p$ . The brown line is the median  $V_c$  in a linear scale against  $z - z_p$ . The two scale heights for each ion species in the upper right corner are calculated  $\pm 50$  km altitude within the PEB and  $[-300, -200]$  km below the PEB, respectively.

words, on both sides of the PEB, magnetic pressure dominates, and the PEB is not a boundary that the ionospheric plasma pressure balances with the magnetic pressure as at Venus. Meanwhile, as shown in Figures 1, 2, 5, and Figure S2 in Supporting Information S1, the magnetic field does not show a sharp change in amplitude across the PEB. To further illustrate this point, we calculate the magnetic ratio near the PEB, more specifically the 95%-rank  $|B|$  divided by the 5%-rank  $|B|$  within the PEB  $\pm 50$  km. The distribution of this magnetic ratio is shown in Figure 7b, which peaks near one and has a median value of 1.11. In short, near the PEB, the magnetic pressure dominates over ionospheric thermal pressure, and there is no obvious change in  $P_B$  across the PEB either. It suggests that the PEB is not a pressure balance boundary between  $P_{th}$  and  $P_B$ , nor is it the result of force balance between  $\nabla P_{th}$  and  $\nabla P_B$ .

We, therefore, focus on examining the ratio between the cold planetary plasma pressure and the magnetic pressure near and below the PEB. The temperatures of the cold ionospheric electrons and ions can be derived from measurements by the Langmuir Probe and Waves (LPW) instrument (Andersson et al., 2015) and STATIC, respectively. Hanley et al. (2021) used STATIC measurements to derive ion temperatures for  $O_2^+$  ( $T_{O_2^+}$ ) from periaapsis to  $\sim 500$  km altitude, above which spacecraft and APP reorientation prevent the application of their technique. From 300 to 500 km altitude on the dayside, they found  $O_2^+$  core temperatures of order 0.1 eV, although suprathermal tails were also present in most of the distributions. For simplicity and to account for the contribution of suprathermal tails to the total ion pressure, we use 1 eV as an upper limit for both electron (Ergun et al., 2021) and ion (Fowler et al., 2022b) temperatures and the total ion density from the STATIC L3 products (provided at Ion Mass 1, 2, 16, 32, and 44) to be the plasma density to calculate the plasma pressure of the cold planetary plasma  $P_{th}$ . As shown later, we do not require high accuracy in the estimates of  $P_{th}$  as it is much smaller than  $P_B$ .

Figure 7a illustrates the distributions of maximum  $P_{th}/P_B$  (95%-rank, red) and minimum  $P_{th}/P_B$  (5%-rank, blue) within PEB  $\pm 50$  km altitude (similar to Figure 5), which shows a median ratio of  $\sim 0.05$  and  $\sim 0.015$ , respectively. That is, within the vicinity of the PEB, the magnetic pressure is more than one order of magnitude higher than the thermal plasma pressure. In other

#### 4.4. PEB and Characteristic Velocity of Sheath Flow

What determines the location of the PEB? Another feature observed in the case studies is that the PEB is located where the hot sheath plasma flow sharply “turns” cold and stagnate (ions having low energies and a narrow energy width, possibly mainly planetary protons), signified by  $V_c$  approaching 0. Figure 8a shows the median  $V_c$  above (red), at (black), and below (blue) the PEB as a function of SZA, which are  $\sim 200$ ,  $\sim 100$ , and  $\sim 50$  km/s, equivalent of a proton energy of  $\sim 200$ ,  $\sim 50$ , and  $\sim 10$  eV, respectively. In Figure 8b, we map the median  $V_c$  as a function of altitude and SZA, overlaid with empirical locations of the bow shock and the MPB (black and cyan dashed lines; Vignes et al., 2000) and the calculated median PEB altitudes (magenta line). Right across the PEB,  $V_c$  sharply decreases from hundreds of km/s to less than 100 km/s. In Figure 8c, we plot the median  $V_c$  within SZA =  $[20^\circ, 30^\circ]$  against altitude, overlaid with these three boundaries as the horizontal dashed lines. We can see that  $V_c$  is over 400 km/s upstream of the bow shock, then decreases to 200–300 km/s in the magnetosheath, and has another sharp decrease from the MPB to the PEB. Similarly, the brown line in Figure 5 shows  $V_c$  sharply decreases from  $>200$  km/s to  $\sim 20$  km/s across the PEB. This sharp reduction in  $V_c$  near the PEB echoes the transition from a hot sheath plasma flow to the cold and slow (small  $V_c$ ) population (mainly

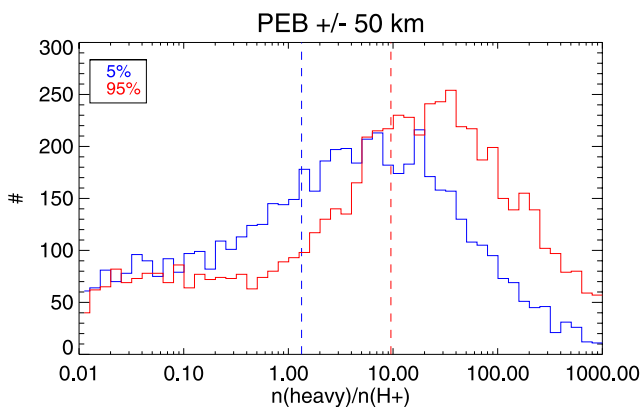


**Figure 6.** The distribution of the ratios of heavy ion densities  $(n(O^+) + n(O_2^+))$  and proton densities within the photoelectron boundary (PEB)  $\pm 50$  km altitude. For each PEB crossing, minimum (5%-rank) and maximum (95%-rank) density ratios are cataloged. The red line shows the distribution of maximum density ratios and blue for minimum density ratios. The two vertical lines mark the median value of each distribution.

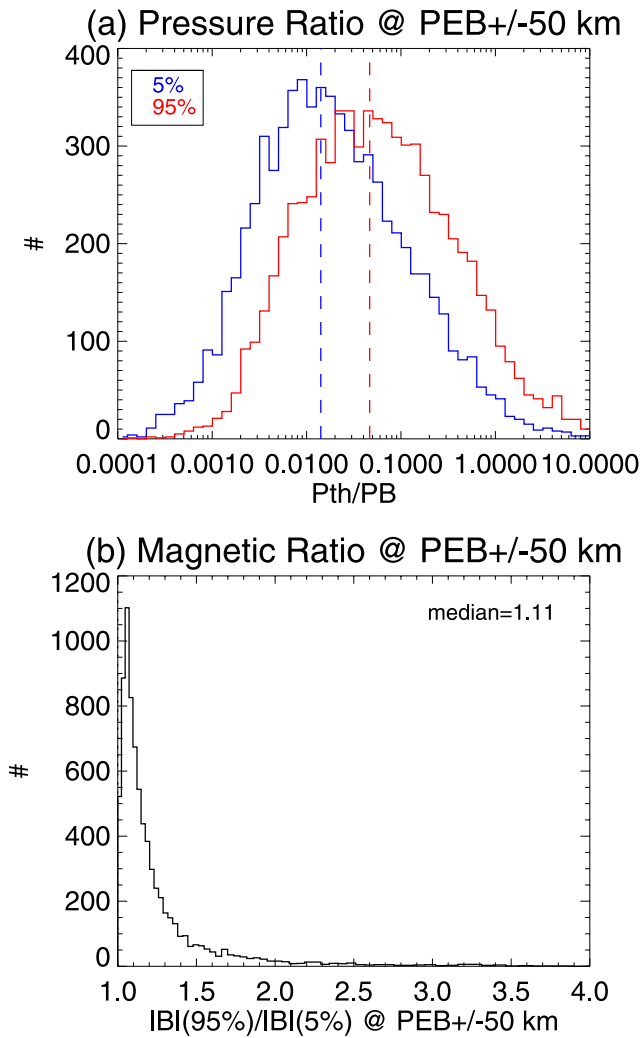


**Figure 7.** (a) The distribution of pressure ratios (plasma  $\beta$ ), thermal plasma pressure divided by magnetic pressure, within photoelectron boundary (PEB)  $\pm 50$  km altitude. The red line shows the distribution of maximum pressure ratios (95%-rank) and blue for minimum pressure ratios (5%-rank). The two vertical lines mark the median values of each distribution. (b) Magnetic ratio near the PEB, more specifically 95%-rank  $IBI$  divided by the 5%-rank  $IBI$  within PEB  $\pm 50$  km.

planetary protons) shown in the case studies (Figures 1b and 2b). Note that  $V_c$  does not exactly go down to 0 likely because planetary protons have significant thermal and/or bulk velocities. In short, the PEB separates regions dominated by mainly solar wind protons to mainly planetary ions and is located where solar wind protons stop penetrating deeper into the ionosphere.

## 5. Physical Interpretation

In previous sections, we have demonstrated the following characteristics of the PEB using both case studies and the statistical analysis of many orbits: (a) the PEB altitude is strongly correlated with the crustal magnetic field strength and increases with SZA; (b) large heavy ion density gradients occur at the PEB; (c) the PEB falls within the ICB (i.e., a switch in the ion composition is observed near the PEB); (d) the PEB is not a boundary where the dominant pressure terms change across the boundary but is dominated by magnetic pressure on both sides; (e) the characteristic ion velocity  $V_c$  sharply decreases to small values across the PEB. To synthesize these aspects, we illustrate our physical interpretation in a schematic shown in Figure 9.

The PEB marks a topological transition from magnetic field lines having access to the ionosphere (open or closed topology) to not having access (draped topology). Above the main ion production region that extends from the main peak ( $\sim 120$ – $180$  km) to the exobase ( $\sim 200$  km), in situ ion production is insignificant compared to diffusion/transport from below, such that high-altitude ion densities are strongly affected by the magnetic connectivity to the production region. With ionospheric magnetic field strengths typically greater than 30 nT, cold planetary ions ( $kT < \text{few eV}$ ) are magnetized above the exobase, so they can easily diffuse along closed or open field lines from the main ionosphere to high altitudes. In contrast, for draped fields with no direct access to the main ionosphere, cold planetary ions must drift across field lines to get on draped field lines, which occur far too slowly to be significant. This explains why large ion density gradients occur near the PEB and also why the PEB falls within the ICB. Therefore, at Mars where the concept of a conventional ionopause is not normally applicable, the PEB can be considered as the top of the dayside ionosphere.

We have shown that the PEB does not result from pressure balance between the magnetic pressure and plasma thermal pressure. Meanwhile, the characteristic velocity of the shocked solar wind flow  $V_c$  decreases significantly across the PEB, indicative of the transition from a hot sheath plasma flow to cold, slow-moving (likely planetary) ion populations. In other words, the PEB is located where the shocked solar wind flow stops penetrating toward

the planet. Our interpretation is that the PEB is the top of the dayside ionosphere and also the interface where the sheath flow diverts around the planet.

It is instructive to compare the pressure terms and plasma boundaries at Venus and Mars, as illustrated in the schematic in Figure 10. As discussed above, at Venus, particularly during solar maximum, the ionospheric thermal pressure above the exobase is strong enough to balance (stand off) the magnetic pressure in the magnetic pileup region (MPR), creating an ionopause that separates the ionosphere from the MPR. In contrast, the ionospheric thermal pressure above the exobase at Mars is usually insufficient to balance the magnetic pressure of the MPR. However, a topological boundary, the PEB, occurs nonetheless, which plays a similar role to an ionopause in that it separates cold ionospheric plasma from the overlying sheath plasma, and defines the boundary around which the sheath plasma flows. Another possibly related difference between Mars and Venus is that the thickness of Mars's magnetosheath is of the order of a solar proton gyro-radius ( $R_L$ ) in contrast to a thickness of multiple  $R_L$  at Venus (Ledvina et al., 2008). This means that Mars's magnetosheath does not have sufficient room for the solar wind to fully thermalize and thus kinetic physics is more important in this region at Mars than at Venus,

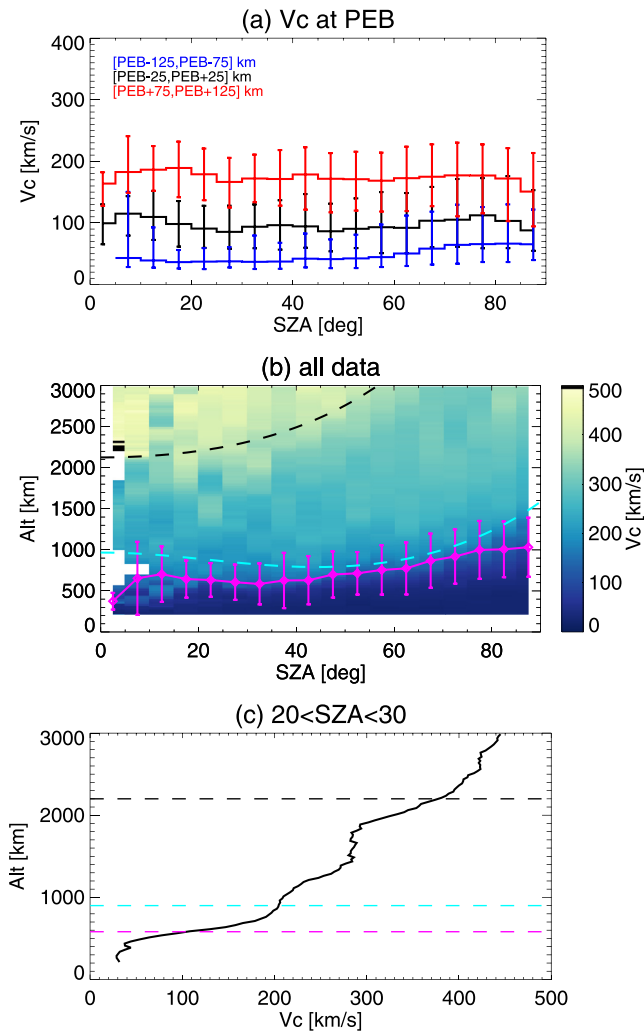


**Figure 8.** (a) Median  $V_c$  above (red), at (black), and below (blue) the photoelectron boundary (PEB) as a function of solar zenith angle (SZA), with vertical bars being the quartiles. (b) Median  $V_c$  against altitude and SZA. The black and cyan dashed lines are the empirical bow shock and magnetic pileup boundary (MPB) locations (Vignes et al., 2000), respectively, and the magenta lines are the median (and the first and third quartiles as error bars) PEB altitude against SZA. (c) The black line is the median  $V_c$  as a function of altitude and the three dashed lines mark the altitude for the empirical bow shock (black) and MPB (cyan) locations and median PEB altitude (magenta) within  $\text{SZA} = [20^\circ, 30^\circ]$ .

which may affect the formation of boundaries between the ionosphere and the magnetosheath (Dubinin et al., 1993; Moses et al., 1988). It might be interesting to compare these regions and boundaries at both Mars and Venus in more detail.

As shown above, there is no balance between  $\nabla P_B$  and sheath plasma pressure gradient  $\nabla P_{th}$  near the PEB. We infer the cause of the sheath flow diverting around the PEB using a two-fluid (the solar wind protons and heavy planetary ions) approximation (Chapman & Dunlop, 1986; Halekas et al., 2017; Ma et al., 2019; Sauer et al., 1994). With  $P_B$  dominating both sides of the PEB (assuming negligible  $\mathbf{J} \times \mathbf{B}$ ), the remaining ion force terms on the sheath flow are momentum exchange between planetary ions and sheath protons, the electron pressure gradient, and the sheath proton pressure gradient. Thus, the PEB likely results from a combination of momentum exchange between the sheath flow and planetary ions and the ionospheric electron pressure gradient that balance the sheath plasma pressure gradient (already much reduced because of the magnetic gradient near the MPB). This may be investigated with MHD simulations or carefully selected case studies where electron and ion moments can be derived reliably with MAVEN data; however, this is beyond the scope of our study.

A noteworthy implication of magnetic pressure dominating below the PEB (Figure 10b) is that the ionosphere can be magnetized without the solar wind plasma carrying the magnetic fields. These induced magnetic fields should instead mainly be generated by ionospheric currents. This is to say that the PEB is not necessarily the inner boundary of the MPR—another major difference between the PEB and the conventional ionopause.

It is also worth noting that the physical pictures provided in Figures 9 and 10 are more suitable for planetary ions remaining relatively cold ( $< \text{a few eV}$ ) near the PEB. When planetary ions are significantly energized and hot, for example, when the upstream IMF is nearly radial (Fowler et al., 2022a), these ions are likely unmagnetized so that magnetic topology matters less, and this scenario is not necessarily applicable.

## 6. Discussion

There have been numerous studies dedicated to characterizing plasma boundaries at Mars. As these boundaries are mostly observation-based, different conclusions might be reached depending on the specific definitions, especially when a particular threshold is chosen and the boundary is identified as one particular location. As this is not a review paper, we limit this discussion to a few studies that are relevant to our results.

Studies have shown that the ICB is generally located at or below MPB (Matsunaga et al., 2017) and the PEB is located below the ICB (Holmberg et al., 2019). As discussed above, the PEB is a topological boundary with a negligible thickness (electron gyroradius  $\sim 1$  km) while the ICB is a boundary with a significant thickness (Halekas et al., 2018), as the ion gyroradius is much larger (tens to hundreds of km) and cold planetary ions can also diffuse across magnetic field lines (although at a much slower rate than field-aligned diffusion). Therefore, our conclusion of the PEB falling within the ICB is not contradictory to previous studies considering ICB's thickness.

There have been prior studies characterizing the relation between the “ionopause” and the PEB at Mars (Chu et al., 2021, 2019; Duru et al., 2009; Han et al., 2014). Most of the studies of the ionopause at Mars have definitions different from the conventional definition at Venus (both a sharp plasma density gradient (thus thermal pressure gradient) and magnetic pressure gradient), mainly defined based on the sharp gradient in electron density (Chu et al., 2021, 2019; Duru et al., 2009; Sánchez-Cano et al., 2020) or in ion density (Vogt et al., 2015) or the

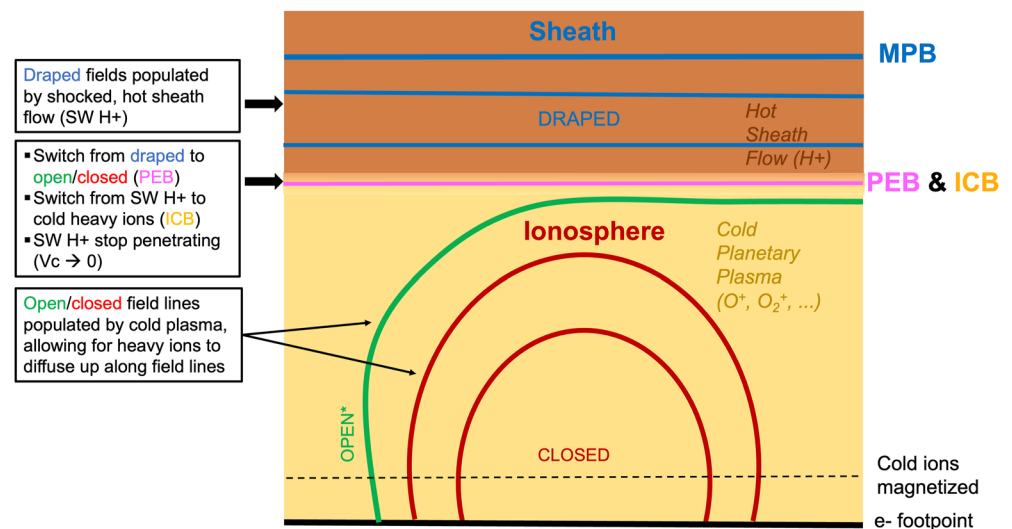


**Figure 9.** A schematic that synthesizes our physical interpretation.

altitude of a certain density (Han et al., 2014). A few key conclusions from these studies are: (a) the ionopause is only occasionally observed (Duru et al., 2009; Sánchez-Cano et al., 2020; Vogt et al., 2015); (b) the ionopause is sometimes observed to be co-located with the PEB (Duru et al., 2009); (c) the ionopause is generally located at  $\sim 200$  km below the PEB (Chu et al., 2019, 2021; Han et al., 2014).

To reconcile previous studies with our results, a few factors should be considered. First, a prominent difference between our study and previous studies is that we identify the PEB based on the energy-pitch angle distribution and not just the energy distribution, as this is a topological boundary. More specifically, we define the PEB to be the transition from closed/open topology to draped topology, while previous studies used electron energy spectrograms to separate photoelectrons and sheath electrons, which could be ambiguous when both populations are present on open field lines. As both closed and open field lines have access to the main ionosphere, allowing planetary cold ions to diffuse upward, it is important to have the capability to clearly distinguish these topologies.

Second, previous studies of the ionopause are largely limited to low altitudes ( $< 500$ – $600$  km) because of the measurement limitations: (a) electron densities measured by the Mars Advanced Radar for Subsurface and Ionosphere Sounding onboard Mars Express have a lower limit of  $1.24 \times 10^2 \text{ cm}^{-3}$  (Gurnett et al., 2008) (used by Chu et al., 2021, 2019; Duru et al., 2009; Han et al., 2014); (b) electron densities measured by the LPW instrument (Andersson et al., 2015) onboard MAVEN have a lower limit of  $\sim 20 \text{ cm}^{-3}$  (used by Fowler et al., 2019; Sánchez-Cano et al., 2020); (c) ion densities measured by the Neutral Gas and Ion Mass Spectrometer (NGIMS; Mahaffy et al., 2015) become less reliable above 300–400 km where ion transport can easily cause ions not to be captured by NGIMS's narrow FOV (used by Vogt et al., 2015). These limitations mean that only low-altitude events with sufficiently large densities can be identified. As pointed out by Fowler et al. (2019) and Sánchez-Cano et al. (2020), sharp density gradients identified at low altitudes are more likely to occur during high dynamic pressure periods. In contrast, the usage of STATIC ion data allows us to accurately determine ion densities down to  $< 1 \text{ cm}^{-3}$  so that density gradients can be identified up to  $> 1000$  km altitude. In addition, instead of searching for “sharp” density gradients, we focus more on the fact that the ion density gradient is much larger across the PEB than below the PEB. With the additional feature that the heavy-ion-to-proton density ratio changes drastically across the PEB, we argue that the PEB marks the transition between cold planetary ions and hot sheath flow, and can thus be considered to be the top of the dayside Mars ionosphere.

In regard to what determines the location of the PEB, our results show the PEB is not where the dominant pressure term changes. This is consistent with findings in Holmberg et al. (2019), where they show pressure balance between the magnetic pressure and the ionospheric plasma pressure occurs below the PEB and ICB. Instead, our analysis reveals that the PEB is located where the hot sheath flow experiences a significant reduction in its characteristic velocity, transitioning to the cold and slow planetary ion flow.



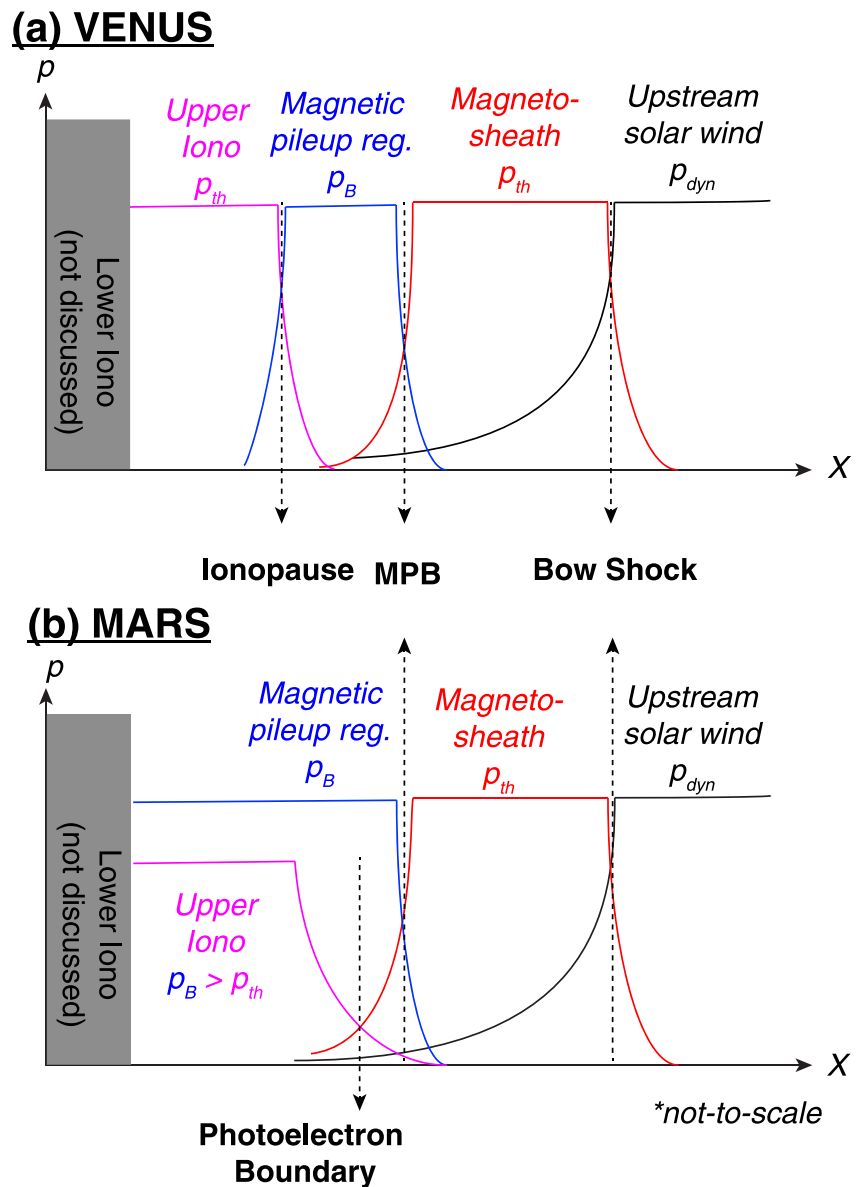


**Figure 10.** A schematic comparing the pressure balance along the sub-solar line at Venus and Mars, as well as typical boundaries. The Venus cartoon is for the solar maximum condition. Both panels are not to scale and the pressure terms are not discussed in the lower ionosphere.

### 7. Concluding Remarks

In this study, we characterize the dayside PEB as the highest altitude where the magnetic topology changes from open/closed to draped, marking a transition from magnetic field lines “having” to “not having” access to the dayside main ionosphere. Our selected PEBs show similar properties to those of previous studies, such as a strong control by Mars’s crustal magnetic fields and an altitude that increases with SZA. The main purpose of this paper is to explore the physical nature of this boundary. First, large planetary ion density gradients occur across the PEB, and PEB falls within the ICB. This can be explained since cold planetary ions are largely magnetized so that the PEB is a good separator between magnetic field lines populated mainly by cold planetary ions when they are connected to the main ionosphere (open or closed) and otherwise populated mainly by the hot sheath plasma. We thus reason that the PEB can be considered as the top of the Mars dayside ionosphere. Second, our results show that the PEB does not result from a balance boundary between magnetic pressure and thermal plasma pressure. Instead, magnetic pressure dominates on both sides. Meanwhile, we find that the PEB is located where

the characteristic velocity of the proton flow sharply decreases to small values, corresponding to the transition from hot sheath plasma flow to cold planetary ion flow, or where the shocked solar wind flow diverts around the planet. In short, this study does not focus on the comparison of the exact locations of different boundaries but more emphasizes the physical explanation of why these phenomena occur at similar locations.

## Data Availability Statement

The MAVEN data used in this study are available through the Planetary Data System (<https://pds-ppi.igpp.ucla.edu/mission/MAVEN>).

## Acknowledgments

This work was supported by the National Aeronautics and Space Administration (NASA) grant NNH10CC04C to the University of Colorado and by subcontract to Space Sciences Laboratory, University of California, Berkeley. The MAVEN project is supported by NASA through the Mars Exploration Program. S. Xu, S. M. Curry, and D. L. Mitchell also acknowledge support from NASA's Mars Data Analysis Program, Grant 80NSSC17K0455. Parts of this work for the observations obtained with the SWEA instrument are supported by the French space agency CNES (National Centre for Space Studies).

## References

- Acuña, M., Connerney, J., Wasilewski, P. A., Lin, R., Anderson, K., Carlson, C., et al. (1998). Magnetic field and plasma observations at Mars: Initial results of the Mars Global Surveyor mission. *Science*, 279(5357), 1676–1680. <https://doi.org/10.1126/science.279.5357.1676>
- Andersson, L., Ergun, R., Delory, G., Eriksson, A., Westfall, J., Reed, H., et al. (2015). The Langmuir probe and waves (LPW) instrument for MAVEN. *Space Science Reviews*, 195(1–4), 173–198. <https://doi.org/10.1007/s11214-015-0194-3>
- Bertucci, C., Duru, F., Edberg, N., Fraenz, M., Martinecz, C., Szego, K., & Vaisberg, O. (2012). The induced magnetospheres of Mars, Venus, and Titan. In *The plasma environment of Venus, Mars, and Titan* (pp. 113–171). Springer.
- Bertucci, C., Mazelle, C., Acuna, M., Russell, C., & Slavin, J. (2005). Structure of the magnetic pileup boundary at Mars and Venus. *Journal of Geophysical Research: Space Physics*, 110(A1), A01209. <https://doi.org/10.1029/2004ja010592>
- Chapman, S., & Dunlop, M. (1986). Ordering of momentum transfer along  $\nabla v_B$  in the AMPTE solar wind releases. *Journal of Geophysical Research: Space Physics*, 91(A7), 8051–8055. <https://doi.org/10.1029/ja091ia07p08051>
- Chu, F., Girazian, Z., Duru, F., Ramstad, R., Halekas, J., Gurnett, D., et al. (2021). The dayside ionopause of Mars: Solar wind interaction, pressure balance, and comparisons with Venus. *Journal of Geophysical Research: Planets*, 126(11), e2021JE006936. <https://doi.org/10.1029/2021je006936>
- Chu, F., Girazian, Z., Gurnett, D., Morgan, D., Halekas, J., Kopf, A., et al. (2019). The effects of crustal magnetic fields and solar EUV flux on ionopause formation at Mars. *Geophysical Research Letters*, 46(17–18), 10257–10266. <https://doi.org/10.1029/2019gl083499>
- Connerney, J., Acuña, M., Ness, N., Kletetschka, G., Mitchell, D., Lin, R., & Reme, H. (2005). Tectonic implications of Mars crustal magnetism. *Proceedings of the National Academy of Sciences of the United States of America*, 102(42), 14970–14975. <https://doi.org/10.1073/pnas.0507469102>
- Connerney, J., Espley, J., Lawton, P., Murphy, S., Odom, J., Oliverson, R., & Sheppard, D. (2015). The MAVEN magnetic field investigation. *Space Science Reviews*, 195(1–4), 1–35. <https://doi.org/10.1007/s11214-015-0169-4>
- Crider, D., Cloutier, P., Law, C., Walker, P., Chen, Y., Acuña, M., et al. (2000). Evidence of electron impact ionization in the magnetic pileup boundary of Mars. *Geophysical Research Letters*, 27(1), 45–48. <https://doi.org/10.1029/1999GL003625>
- Dubinin, E., Fränz, M., Woch, J., Roussos, E., Barabash, S., Lundin, R., et al. (2006). Plasma morphology at Mars. ASPERA-3 observations. *Space Science Reviews*, 126(1–4), 209–238. <https://doi.org/10.1007/s11214-006-9039-4>
- Dubinin, E., Lundin, R., Koskinen, H., & Norberg, O. (1993). Cold ions at the Martian bow shock: Phobos observations. *Journal of Geophysical Research: Space Physics*, 98(A4), 5617–5623. <https://doi.org/10.1029/92ja02374>
- Duru, F., Gurnett, D., Frahm, R., Winningham, J., Morgan, D., & Howes, G. (2009). Steep, transient density gradients in the Martian ionosphere similar to the ionopause at Venus. *Journal of Geophysical Research: Space Physics*, 114(A12). <https://doi.org/10.1029/2009ja014711>
- Ergun, R., Andersson, L., Fowler, C., Thaller, S., & Yelle, R. (2021). In situ measurements of electron temperature and density in Mars' dayside ionosphere. *Geophysical Research Letters*, 48(14), e2021GL093623. <https://doi.org/10.1029/2021gl093623>
- Fowler, C. M., Hanley, K., McFadden, J., Halekas, J., Schwartz, S., Mazelle, C., et al. (2022a). A MAVEN case study of radial IMF at Mars: Impacts on the dayside ionosphere. *Journal of Geophysical Research: Space Physics*, 127, e2022JA030726.
- Fowler, C. M., Lee, C., Xu, S., Mitchell, D., Lillis, R., Weber, T., et al. (2019). The penetration of draped magnetic field into the Martian upper ionosphere and correlations with upstream solar wind dynamic pressure. *Journal of Geophysical Research: Space Physics*, 124(4), 3021–3035. <https://doi.org/10.1029/2019ja026550>
- Fowler, C. M., McFadden, J., Hanley, K., Mitchell, D. L., Curry, S., & Jakosky, B. (2022b). In situ measurements of ion density in the Martian ionosphere: Underlying structure and variability observed by the MAVEN-STATIC instrument. *Journal of Geophysical Research: Space Physics*, 127, e2022JA030352. <https://doi.org/10.1029/2022JA030352>
- Frahm, R., Sharber, J., Winningham, J., Wurz, P., Liemohn, M., Kallio, E., et al. (2006). Locations of atmospheric photoelectron energy peaks within the Mars environment. *Space Science Reviews*, 126(1–4), 389–402. <https://doi.org/10.1007/s11214-006-9119-5>
- Garnier, P., Steckiewicz, M., Mazelle, C., Xu, S., Mitchell, D., Holmberg, M. K. G., et al. (2017). The Martian photoelectron boundary as seen by MAVEN. *Journal of Geophysical Research: Space Physics*, 122(10), 10472–10485. <https://doi.org/10.1002/2017ja024497>
- Gurnett, D. A., Huff, R. L., Morgan, D. D., Persoon, A. M., Averkamp, T. F., Kirchner, D. L., et al. (2008). An overview of radar soundings of the Martian ionosphere from the Mars Express spacecraft. *Advances in Space Research*, 41(9), 1335–1346. <https://doi.org/10.1016/j.asr.2007.01.062>
- Halekas, J., Brain, D., Luhmann, J., DiBraccio, G., Ruhunusiri, S., Harada, Y., et al. (2017). Flows, fields, and forces in the Mars-solar wind interaction. *Journal of Geophysical Research: Space Physics*, 122(11). <https://doi.org/10.1002/2017ja024772>
- Halekas, J., McFadden, J., Brain, D., Luhmann, J., DiBraccio, G., Connerney, J., et al. (2018). Structure and variability of the Martian ion composition boundary layer. *Journal of Geophysical Research: Space Physics*, 123(10), 8439–8458. <https://doi.org/10.1029/2018ja025866>
- Halekas, J., Taylor, E., Dalton, G., Johnson, G., Curtis, D., McFadden, J., et al. (2015). The solar wind ion analyzer for MAVEN. *Space Science Reviews*, 195(1–4), 125–151. <https://doi.org/10.1007/s11214-013-0029-z>
- Han, X., Fraenz, M., Dubinin, E., Wei, Y.-j., Andrews, D. J., Wan, W., et al. (2014). Discrepancy between ionopause and photoelectron boundary determined from Mars express measurements. *Geophysical Research Letters*, 41(23), 8221–8227. <https://doi.org/10.1002/2014gl062287>
- Hanley, K. G., McFadden, J. P., Mitchell, D. L., Fowler, C. M., Stone, S. W., Yelle, R., et al. (2021). In situ measurements of thermal ion temperature in the Martian ionosphere. *Journal of Geophysical Research: Space Physics*, 126(12), e2021JA029531. <https://doi.org/10.1029/2021ja029531>
- Holmberg, M. K., Andre, N., Garnier, P., Modolo, R., Andersson, L., Halekas, J., et al. (2019). MAVEN and MEX multi-instrument study of the dayside of the Martian induced magnetospheric structure revealed by pressure analyses. *Journal of Geophysical Research: Space Physics*, 124(11), 8564–8589. <https://doi.org/10.1029/2019ja026954>

- Ledvina, S., Ma, Y.-J., & Kallio, E. (2008). Modeling and simulating flowing plasmas and related phenomena. In *Comparative aeronomy* (pp. 143–189). Springer.
- Luhmann, J. (1986). The solar wind interaction with Venus. *Space Science Reviews*, *44*(3–4), 241–306. <https://doi.org/10.1007/bf00200818>
- Ma, Y. J., Dong, C. F., Toth, G., van der Holst, B., Nagy, A. F., Russell, C. T., et al. (2019). Importance of ambipolar electric field in driving ion loss from Mars: Results from a multifluid MHD model with the electron pressure equation included. *Journal of Geophysical Research: Space Physics*, *124*(11), 9040–9057. <https://doi.org/10.1029/2019JA027091>
- Mahaffy, P. R., Benna, M., King, T., Harpold, D. N., Arvey, R., Barciniak, M., et al. (2015). The neutral gas and ion mass spectrometer on the Mars atmosphere and volatile evolution mission. *Space Science Reviews*, *195*(1–4), 49–73. <https://doi.org/10.1007/s11214-014-0091-1>
- Matsunaga, K., Seki, K., Brain, D. A., Hara, T., Masunaga, K., McFadden, J. P., et al. (2017). Statistical study of relations between the induced magnetosphere, ion composition, and pressure balance boundaries around Mars based on MAVEN observations. *Journal of Geophysical Research: Space Physics*, *122*(9), 9723–9737. <https://doi.org/10.1002/2017ja024217>
- McFadden, J., Kortmann, O., Curtis, D., Dalton, G., Johnson, G., Abiad, R., et al. (2015). MAVEN suprathermal and thermal ion composition (STATIC) instrument. *Space Science Reviews*, *195*(1–4), 199–256. <https://doi.org/10.1007/s11214-015-0175-6>
- Mitchell, D., Lin, R., Mazelle, C., Reme, H., Cloutier, P., Connerney, J., et al. (2001). Probing Mars' crustal magnetic field and ionosphere with the MGS Electron Reflectometer. *Journal of Geophysical Research: Planets (1991–2012)*, *106*(E10), 23419–23427. <https://doi.org/10.1029/2000je001435>
- Mitchell, D., Mazelle, C., Sauvaud, J.-A., Thocaven, J.-J., Rouzaud, J., Fedorov, A., et al. (2016). The MAVEN solar wind electron analyzer. *Space Science Reviews*, *200*(1–4), 495–528. <https://doi.org/10.1007/s11214-015-0232-1>
- Morschhauser, A., Lesur, V., & Grott, M. (2014). A spherical harmonic model of the lithospheric magnetic field of Mars. *Journal of Geophysical Research: Planets*, *119*(6), 1162–1188. <https://doi.org/10.1002/2013je004555>
- Moses, S., Coroniti, F., & Scarf, F. (1988). Expectations for the microphysics of the Mars-solar wind interaction. *Geophysical Research Letters*, *15*(5), 429–432. <https://doi.org/10.1029/g1015i005p00429>
- Nagy, A., Winterhalter, D., Sauer, K., Cravens, T., Brecht, S., Mazelle, C., et al. (2004). The plasma environment of Mars. In *Mars' magnetism and its interaction with the solar wind* (pp. 33–114). Springer.
- Sánchez-Cano, B., Narvaez, C., Lester, M., Mendillo, M., Mayyasi, M., Holmstrom, M., et al. (2020). Mars' ionopause: A matter of pressures. *Journal of Geophysical Research: Space Physics*, *125*(9), e2020JA028145. <https://doi.org/10.1029/2020ja028145>
- Sauer, K., Bogdanov, A., & Baumgärtel, K. (1994). Evidence of an ion composition boundary (protonopause) in bi-ion fluid simulations of solar wind mass loading. *Geophysical Research Letters*, *21*(20), 2255–2258. <https://doi.org/10.1029/94gl01691>
- Vignes, D., Mazelle, C., Rme, H., Acuña, M. H., Connerney, J. E. P., Lin, R. P., et al. (2000). The solar wind interaction with Mars: Locations and shapes of the bow shock and the magnetic pileup boundary from the observations of the MAG/ER Experiment onboard Mars Global Surveyor. *Geophysical Research Letters*, *27*(1), 49–52. <https://doi.org/10.1029/1999GL010703>
- Vogt, M. F., Withers, P., Mahaffy, P. R., Benna, M., Elrod, M. K., Halekas, J. S., et al. (2015). Ionopause-like density gradients in the Martian ionosphere: A first look with MAVEN. *Geophysical Research Letters*, *42*(21), 8885–8893. <https://doi.org/10.1002/2015gl065269>
- Wang, Y., Cao, Y., Cui, J., Wei, Y., & Rong, Z. (2022). An automatic identification method for the photoelectron boundary at Mars. *The Astrophysical Journal*, *163*(4), 186. <https://doi.org/10.3847/1538-3881/ac5825>
- Xu, S., Liemohn, M. W., Dong, C., Mitchell, D. L., Bougher, S. W., & Ma, Y. (2016). Pressure and ion composition boundaries at Mars. *Journal of Geophysical Research: Space Physics*, *121*(7), 6417–6429. <https://doi.org/10.1002/2016ja022644>
- Xu, S., Weber, T., Mitchell, D. L., Brain, D. A., Mazelle, C., DiBraccio, G. A., & Espley, J. (2019). A technique to infer magnetic topology at Mars and its application to the terminator region. *Journal of Geophysical Research: Space Physics*, *124*(3), 1823–1842. <https://doi.org/10.1029/2018ja026366>